Submitted to **Journal Title** [Digital micromirror device characterisation for ultrashort laser applications]
Template provided by EDP Sciences

Research papers

Digital micromirror device characterisation for ultrashort laser applications

Mitzi Ordoñez-Perez [1*], Pedro J. Clemente-Pesudo[1,2], Francis Rey U. Cortes[1], Jesús Lancis[1], Enrique Tajahuerce[1] and G. Mínguez-Vega[1]

[1] GROC-UJI, Institute of New Imaging Technologies (INIT), Universitat Jaume I, 12071, Castelló, Spain
[2] Servei Central d'Instrumentació Científica (SCIC), Universitat Jaume I, Castelló, Spain.

Abstract – In recent years, the wide variety of digital micromirror device (DMD) applications has extended significantly across various fields of optics, including ultrafast optics. Despite these advances, the interaction between DMDs and ultrashort pulses remains poorly understood. To address this gap, this study presents a comprehensive characterization of the behaviour of a DMD system when interacting with ultrashort laser pulses. In this work, the fluence threshold for multi-shot damage was first determined to be 0.12 J/cm^{-2}. Regarding the temporal effects, the group delay dispersion (GDD) of intrinsic materials was experimentally measured for the zeroth order and was determined to be 190 fs^2. The temporal dispersion introduced by the DMD was then theoretically quantified for higher diffraction orders, showing that it generates a broadening and a spatiotemporal shift that depend on the diffraction order. Concerning spatial effects, the lateral chromatic aberration for a broad wavelength range was analysed, revealing the spatial separation of different wavelength components due to the wavelength dependence of the order of diffraction. Finally, the capability of the DMD to analyse the intensity spatial distribution of the light beam was demonstrated using a single-pixel imaging technique. These findings contribute to the understanding of the effects resulting from the interaction of ultrashort pulses with the DMD, thereby facilitating applications.

Keywords: DMD characterisation, femtosecond lasers, single-pixel imaging

1. Introduction

Controlling the spatial beam profile of a laser using spatial light modulators (SLMs) has become increasingly important in the field of ultrafast lasers due to the numerous advantages it provides. SLMs enable the development of advanced technologies such as digital lasers, which provide on-demand laser modes [1], as well as beam profilers [2], wavefront sensors [3, 4], temporal pulse shapers [5, 6] or delay lines [7] that can reduce costs and enhance the performance and or versatility of conventional systems. Additionally, precise beam control provided by SLMs opens new avenues for scientific exploration, including innovations in laser processing [8, 9], attosecond physics [10], generation of the non-linear effects [11, 12], optical communications [13], and other emerging applications [14, 15]. SLMs can be broadly categorised into liquid crystal displays (LCDs) [16], deformable mirrors [17, 18] and lenses [19], as well as digital micromirror devices (DMDs), each exhibiting distinct advantages and certain limitations. For example, LCDs provide precise control over phase, amplitude, and polarization across approximately one million pixels, with a wavefront depth resolution of 8–12 bits. However, their operating speed is limited, with refresh rates typically ranging from tens to hundreds of hertz. On the other hand, deformable mirrors and lenses are capable of handling higher refresh rates in the kilohertz range compared to LCDs. Due to their low number of actuators (typically 1 to 200), they possess limited spatial precision which makes them suitable primarily for correcting optical aberrations.

Moreover, DMDs combine high spatial resolution in the range of millions of pixels and exceptional speed with refresh rates of several kilohertz. Although they are binary amplitude modulators with limited depth precision and diffraction efficiency, DMDs excel in cost-effectiveness, ease of use, and beam-shaping fidelity compared to LCDs [20]. Thus, DMDs are an ideal choice for ultrafast laser applications, where speed, precision, and robustness play crucial roles.

In recent years, there has been an increase in the number of improvements in ultrashort pulse technologies based on DMD performance, for example, in nanomachining [21], ultrafast imaging [22], and temporal and spatial shaping of femtosecond beams [23-25]. Therefore, the employment of fs pulses requires careful consideration to ensure that the high peak power of the

This provisional PDF is the accepted version. The article should be cited as: J. Eur. Opt. Society-Rapid Publ.,
https://doi.org/10.1051/jeos/2026017

electric fields does not damage the DMD. Then, achieving a complete characterisation of their interaction with ultrashort pulses, particularly femtosecond (fs) pulses, has become a central objective in photonics research.

Although some studies have already investigated the laser-induced damage on DMDs, they were initially focused on continuous sources. For example, the first study of DMD damage was conducted using continuous light, where damage occurred at the intensity of 19 kW/cm² [26]. However, the phenomena associated with continuous light differ from those observed with pulses, where the electronic excitation and the **electron-phonon** coupling become more significant [27]. In this context, previous studies have investigated laser-induced damage thresholds for ns and ps pulse durations. For instance, one study used a 532 nm laser with a 10 ns pulse duration and reported a damage threshold fluence of 0.13 J/cm². The same study also examined picosecond pulses (9.2 ps), for which a fluence of 1.5 J/cm² was determined [28]. In the femtosecond regime, a similar approach has been applied to the material from which the micromirrors are fabricated, aluminium. Although a universally accepted damage threshold for femtosecond pulses in aluminium has not been established, studies provide indicative values. Under a helium atmosphere, the threshold fluence for aluminium has been measured at around 0.4 J/cm² [29], and nanoscale damage has been observed at fluences of 0.06 J/cm² [30]. Thus, in depth investigation of employing ultrashort pulses on the DMD is necessary to address the literature gap. In addition to the evaluation of DMD damage by ultrashort pulses, a deeper understanding of how DMD affects the temporal duration and broadband spectrum of the pulse is also essential to include in the characterisation of DMD-laser interaction.

This study presents a comprehensive characterisation of the interaction between near-infrared fs laser pulses and a DMD. This includes an analysis of the device's fluence threshold within a multi-pulse framework, the measurement of the temporal dispersion introduced by DMD, a theoretical study of the behaviour under ultrafast pulsed lasers and an examination of how the DMD affects the laser's broadband spectrum. To illustrate the capability of the DMD, we employed SPI techniques to retrieve the intensity profile of the ultrafast laser pulse.

2. Multishot laser-induced damage threshold Material and Methods

In this section, we characterise the multishot laser-induced damage threshold (LIDT) of the DMD under ultrafast laser irradiation. But before that, we will first briefly review the characteristics of the DMD and, explain the basic physical processes involved in the DMD-pulsed-laser interaction. Then, a detailed description of the experimental procedure used to determine the LIDT of the DMD is also provided.

The DMD is monolithically fabricated by complementary metal-oxide-semiconductor (CMOS) compatible processes over a single-crystal silicon CMOS static random-access memory (SRAM) cell, a detailed structure is given in ref [31]. Thus, it can be separated onto three layers, according to its thermal properties [32]: The bulk micromirror (a), the silicon (b) and the ceramic (c), shown in Fig. 1.

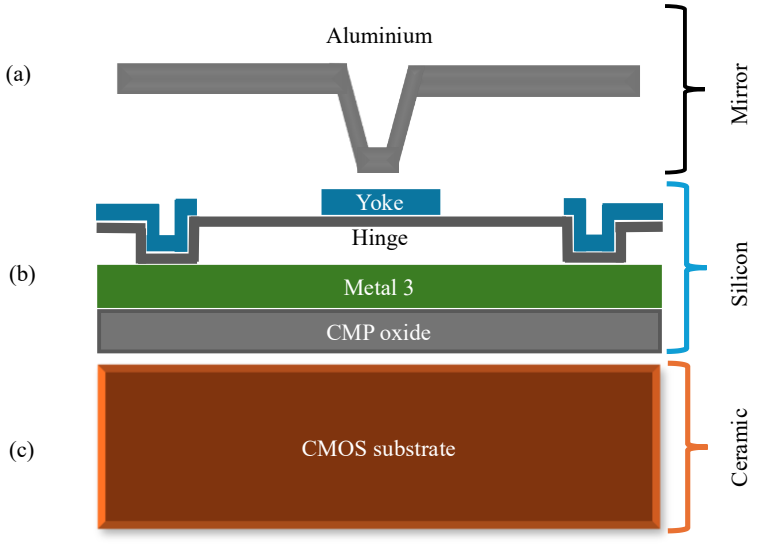

Fig. 1. The bulk mirror refers to the aluminium micromirror, the silicon part contains the yoke, the hinge, the torsion hinge and the micromirror address electrodes, the Metal-3 layer contains are the bias/reset bus, the yoke address electrodes and the via 2 contact to CMOS. The ceramic refers to the memory cell or CMOS SRAM.

The bulk mirror part refers to the aluminium micromirror. The silicon part starts at the yoke, contains the hinge, and the three connected layers, where metal-1 and metal-2 are the underlying interconnects for the third layer, the ceramic, which contains the CMOS memory. Among these layers, the aluminium and silicon-based layers are the sites of various physical processes, which are crucial to understanding the response of the DMD to laser irradiation. Particularly, the aluminium micromirrors have metallic surfaces in which the incident laser energy is primarily absorbed by free electrons. This absorption is then followed by rapid energy relaxation within the electronic subsystem, which subsequently transfers energy to the atomic lattice through electron-**phonon coupling**. Because the electronic heat capacity is much smaller than that of the lattice, the electron temperature can reach very high transient values while maintaining a minimum heat diffusion. Meanwhile, in dielectric materials such as silicon, heat transfer is strongly suppressed. Ultrafast laser ablation of both metals and dielectric materials generally proceeds through multiphoton ionisation and avalanche ionisation to form a neutral plasma, eventually leading to optical breakdown[27, 33]. In previous studies, the aluminium ablation threshold was measured for a 100 fs pulse at 800 nm in a multi-pulse configuration was measured to be 0.52 J/cm^{-2} [34]. In the case of the DMD, the system is more complex, so it is essential to conduct experiments to determine the damage threshold fluence and ensure its durability and long-term stability in ultrafast laser applications.

To determine the laser-induced damage threshold (LIDT) of the DMD, Liu's method was employed [35], which measures the radius of damage on the material's surface as a function of the Gaussian laser beam's fluence. In this method, a beam with a Gaussian profile is considered. Then, the spatial irradiation distribution of a Gaussian beam can be expressed as $\Phi(r)$:

$$\boldsymbol{\Phi(r) = \Phi_{th} \exp\left(-\frac{2r^2}{\rho^2}\right)} \quad (1)$$

Subsequently, assuming the centre of the laser beam coincides with the centre of the damage area $\boldsymbol{A_i}$, the damage threshold fluence $\boldsymbol{\Phi_{th}}$ can be expressed as

$$A(r_i) = 2\pi r_i^2 = \rho^2 In\left[\frac{\Phi}{\Phi_{th}}\right] \quad (2)$$

By adjusting the experimental damage area as a function of fluence using a semilog fit, the threshold fluence can be determined according to Eq. (2).

This experiment was conducted using an ultrafast Ti:sapphire laser (PRO-Compact Femtolaser). The amplifier produces pulses with a duration of around 32 fs at the transform Fourier limit, a central wavelength around of 800 nm, a spectral bandwidth near 30 nm, and operates at a repetition rate of 1 kHz. The DMD used in this study (DMD, DLP7000, Texas Instruments) comprises a 756 x 1024 square micromirror, each with a width of 13.6 um. For the experimental setup, the device was maintained in the off state throughout the measurement of threshold fluences. The experimental arrangement is shown in Fig. 2. Before the focussing lens, a pair of concatenated linear polarisers was used to control the energy level, and a motorised shutter was employed to regulate the exposure time. The mean energy was measured for each pair of polariser angles to obtain the testing points. The shutter exposure time was set to 1 s, corresponding to approximately 1000 pulses per irradiation, according to the laser repetition rate. A convergent lens with a focal length of 550 mm was used to focus the laser beam into the DMD micromirrors surface. The DMD was mounted on a motorised translation stage, allowing precise control of the incident beam position along the X, Y, and Z axes. The motorised XY stage allowed precise lateral positioning of the sample, while the Z axis was used to place the DMD at the focal plane.

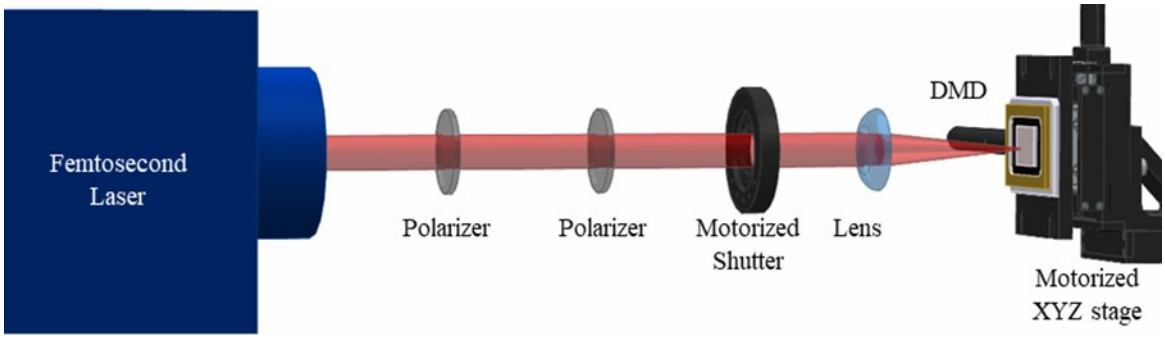

Fig. 2. Schematic diagram of the optical system used to irradiate the DMD. From left to right: femtosecond laser, pair of linear polarisers, motorised shutter, focussing lens, and DMD mounted in a motorised XYZ translation stage.

The incident beam at the focal spot area was meticulously measured, using a commercial beam profiler (WinCam D, Data Array Inc, minimum pixel size 6.45 μm). In our case, the Gaussian beam showed small ellipticity thus, the effective area is obtained instead using the equation as $A_{eff} = \pi\rho_1\rho_2$. Along the horizontal axis, the measured FWHM was 64 ±6 µm and the diameter $(1/e^2)$ was $\rho_1 = 103 \pm 6$ µm. While for the vertical axis, the FWHM was 73 ±6 µm and the diameter $(1/e^2)$ was $2\rho_2 = 123 \pm 6$ µm . Additionally, the focal spot used to irradiate all points on the sample has a value of $9.01\text{x}10^{-4} \pm 0.01\text{x}10^{-4} cm^2$ in air, for the specific focal length used in the experiment. The pulse energy used ranged from 1.4 µJ to 18 µJ. Using a confocal microscope (Sensofar PLu 2300), different planes in the DMD were identified along the optical path. Then, the distance between the external surface of the protective window and the micromirror plane was corroborated to be 2.5 mm, while the glass was confirmed to be 2 mm thick [36]. Thus, in this experiment, the change in the focal spot area due to the window was assumed to be negligible.

Each fluence level was tested at three different positions on the DMD to obtain an average damage-spot size for each fluence value. Three measurements were performed for each fluence, and the average damage area was reported. To measure the damage area, a confocal microscope was used to obtain an image of the irradiated regions, on the DMD`s surface. For an accurate evaluation of the induced damage, initially, greyscale and depth-resolved images (Z-stack) of the DMD's micromirrors were obtained. The addition of Z-stack images provides a higher resolution in identifying damaged micromirrors either by a deviation of their relative planes with neighbouring micromirrors or by a discrepancy in texture or colour.

In Fig. 3 at a fluence of 0.11 J/cm^{-2}, five damaged micromirrors are observed. One missing micromirror is located at the centre of the beam, while the remaining four are at different positions and can be identified as damaged because they lie in a different plane (yellow) from the undamaged micromirrors (orange). Afterward, any deviation from the initial position could affect micromirror functionality, and only the missing micromirrors, as well as darkened micromirrors, were included in the evaluation of the total damaged area shown in Fig. 3. Based on the analysis of the acquired images, no visible damage was observed at fluences below 0.07 J/cm^{-2}. The onset of damage was identified at 0.09 J/cm^{-2}, as shown in Fig. 3, where the first affected micromirror appeared slightly displaced from its plane. At this fluence, a minor deformation type was identified, corresponding to micromirrors that show small displacements while remaining in their original positions within the DMD array, as seen in the greyscale image. The first instance of a completely missing micromirror was observed at 0.10 J/cm², this result is consistent with the recommendation given in the technical notes in reference [37], while symmetrical central damage became evident at fluences exceeding 0.15 J/cm².

According to Lui's method, the experimental damage area is adjusted as a function of fluence using Eq. (2). Under our specific laser conditions, the fluence threshold was identified as $0.12 \pm 0.02\, Jcm^{-2}$, considering the equation $A(r_i) = 1.66x10^{-4}\text{Ln}(\Phi) + 3.54x10^{-4}$. Figure 3 (a) presents the experimental data of damage area as a function of fluence. The point where the damage begins to appear and the corresponding fluence threshold can be appreciated. In Fig. 3 (a), the graph was obtained from 18 different fluence levels, each measured three times. The scatter bars represent the dispersion in the

measured damage areas. The damage was characterised using two types of images: z-stacks of 40 confocal microscope images with 1-µm axial steps (b), and bright-field microscope images (c). The measurements were categorized into three zones, separated by dashed lines: Zone I, Zone II (green line), and Zone III (red line). In Zone I, no damage was observed as illustrated in the first column of images corresponding to fluence of $0.07\,J/cm^{-2}$ (see green point on the graph). In Zone II, the images show apparent damage to the micromirror coating. However, these regions were not considered in the area count. An example is shown in the second column of images, corresponding to a fluence of $0.09\,J/cm^{-2}$ (see red point on the graph). Finally, Zone III refers to the region containing missing micromirrors. The damaged area was quantified by counting the number of missing micromirrors, as shown in the third to fifth columns. The parameters associated with these images are indicated by blue points, corresponding to fluences of $0.11\ J/cm^{-2}$, $0.12\ J/cm^{-2}$, $0.18\,J/cm^{-2}$ of respectively.

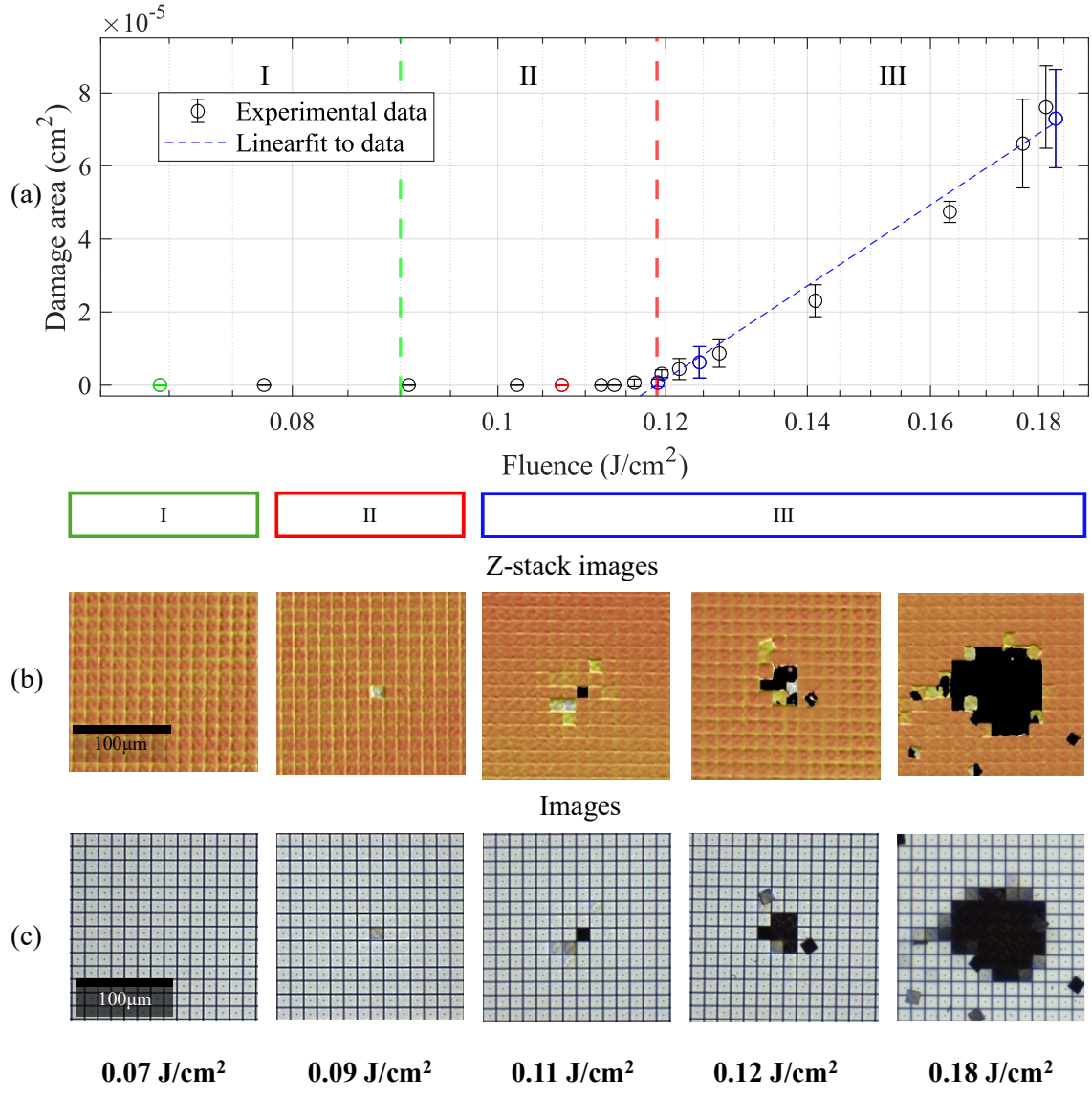

Fig. 3. Damage area as a function of fluence. (a) Experimental measurements taken at 18 fluence levels, each repeated three times; scatter bars indicate variability in the damage area. Three regions are separated by dashed lines: Zone I, where no damage is observed (example at 0.07 J/cm²); Zone II, where apparent coating damage occurs but is not counted (example at 0.09 J/cm²); and Zone III, where missing micromirrors define the quantified damage area (examples at 0.11, 0.12, and 0.18 J/cm²). Damage characterisation uses (b) confocal z-stacks of 40 images with 1-µm steps and (c) bright-field microscopy.

3. Temporal effects

In this section, we analyse the behaviour of ultrashort pulses after interacting with a DMD, and how these effects influence the temporal duration of the pulse. To do this, we first measure the intrinsic dispersion introduced by the DMD materials. Then we theoretically analyse the propagation of the pulsed laser beam after it strikes the DMD surface.

3.1. GDD by DMD

To evaluate the effect of the DMD materials on the laser spectrum, we employed a Ti:Sapphire amplifier (ASTRELLA, Coherent), with a central wavelength of approximately 800 nm, a measured bandwidth of 30 nm, a 31.6 fs pulse at the transform Fourier limit, and a repetition rate of 5kHz. Also, a spectrometer (SC2000 Ocean Optics) was used to measure the spectral distribution of the pulsed beam before and after interaction with the DMD, as show in Fig. 4 (a). The graph presents the normalised intensity (in arbitrary units) as a function of wavelength for both cases. Although the DMD has a negligible impact on the bandwidth because it remains unchanged, the pulse duration increases after passing through the DMD, this behaviour can be attributed to the dispersive characteristics of its constituent materials. The influence of each DMD component on the pulse temporal width was analysed, and the group velocity dispersion (GVD) introduced by the DMD materials was evaluated by comparing the pulse duration before and after reflection. The aluminium of the micromirrors contributes to a reported GVD of 10 fs² [38]. The protective window is then made of alkali borosilicate glass (type 7056) [36], similar to N-BK7 glass, which has a GVD of 44.65 fs² [39]. Consequently, given its thickness of 2 mm the total GDD introduced by the DMD is approximately 190 fs². To verify this estimation, the temporal width of the fs pulses (generated by before and after reflection from the DMD (in the "off" state) was measured using an autocorrelator (Femtolasers Productions GmbH). The pulse duration before reflection was measured to be $(33.1 \pm 1.6) fs$. After reflection, it was $(36.3 \pm 1.6) fs$, according to Fig. 4 (b) and 4 (c) respectively. These results were obtained with the DMD micromirrors in the off state. This result is consistent with the estimated GDD of 190 fs². From the GDD, we theoretically estimate the pulse duration using the pulse elongation equation [40].

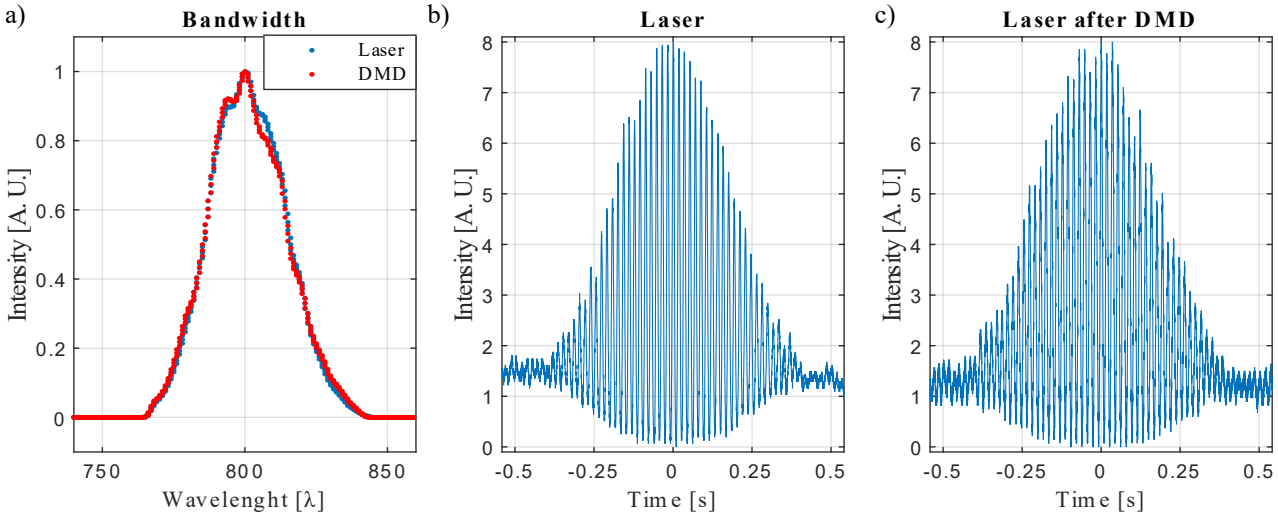

Fig. 4. (a) Normalised spectra of the pulsed laser before (blue) and after (red) reflection from the DMD. Both have a wideband of (30.0 ± 0.6) ***nm*** at FWHM. Analogously, (b) shows the fringe-resolved autocorrelation (FRAC) trace of the input laser pulse, corresponding to a pulse duration of (33.1 ± 1.6) ***fs***, while (c) presents the FRAC autocorrelation of the pulse reflected from the DMD, resulting in a pulse duration of (36.3 ± 1.6) ***fs.***

Theoretical and experimental spatiotemporal dispersion aspects

We also introduce a theoretical model to analyse the spatiotemporal dynamics of the electric field of an ultrashort pulse after its interaction with a digital micromirror device (DMD), based on the general principles of the Huygens–Fresnel integral framework. For simplicity, we initially considered only the X coordinate, assuming symmetry along the Y axis, and a single spectral component with frequency ω within the spectrum. The input electric field profile, is assumed to be Gaussian beam in space and frequency, described by the function $U_{in}(x,\omega) = \exp[-x^2/4\sigma_x^2]\exp[-\omega^2\sigma_t^2]$, where σ_x and σ_t are the width of

spatial and temporal irradiance profiles, respectively, at $\frac{1}{e^2}$. The DMD is modelled as a reflective diffraction grating with period p. For the *mth* diffraction order, under the paraxial approximation, the phase introduced by the DMD can be expressed as Exp $[i\ 2\pi\ m\frac{x'}{p}]$, as reported in [40]. The Huygens–Fresnel diffraction propagation of the beam over a distance L, under the Fraunhofer approximation—that is, considering the far-field diffraction of the DMD—can then be expressed as [41]:

$$U_{out}(x,\omega) = \sqrt{\frac{\omega}{2\pi cLi}}\, exp\left[i\ \frac{\omega L}{c}\right]\int_{-\infty}^{\infty} U_{in}(x,\omega)\ exp\left[-i\frac{\omega}{L\,c}x'\left(x-\frac{2\pi cmL}{p\omega}\right)\right]dx'. \tag{3}$$

In Eq. (3), L denotes the on-axis propagation distance between the input and output planes, and c is the speed of light. After solving the previous integral, and reordering terms, if we omit the square root that represents the intensity factor, we obtain the following,

$$U_{out}(x,\omega) \approx exp\left[i\ \frac{\omega L}{c}\right] exp[-\omega^2\sigma_t^2] * exp\left[-\frac{\left(x-\frac{2\pi cmL}{p\omega}\right)^2}{4\sigma_{x\omega}^2}\right], \tag{4}$$

where $\sigma_{x\omega} = cL/2\ \omega\ \sigma_x$. To simplify the analytical derivation, the first order approximation is applied around ω_0, the central angular frequency of the pulse. This assumption is valid since the pulse bandwidth is a small fraction of the carrier frequency. Under this approximation, the phase term can be expressed as, $\frac{2\pi cmL}{p\omega} \cong \frac{2\pi cmL}{p\omega_0} + \frac{2\pi cmL}{p\omega_0}\frac{\tilde{\omega}}{\omega_0} = \delta_0 + \delta_1\tilde{\omega}$ and $\sigma_{x\omega}^2 \approx \sigma_{x\omega_0}^2$. Furthermore, a first-order Taylor series expansion is applied to the term $\frac{\omega L}{c}$, defined as $\alpha_i = \frac{\partial^i}{\partial\,\omega^i}\left(\frac{\omega L}{c}\right)\Big|_{\omega=\omega_0}$, which yields $\omega L/c = \alpha_0 + \alpha_1\tilde{\omega}$, with $\tilde{\omega} = \omega - \omega_0$, simplifying the first exponential term. By substituting all these approximations into Eq. (4), we obtain the following expression:

$$U_{out}(x,\omega) \approx \exp[i\ (\alpha_0 + \alpha_1\tilde{\omega})]\ \exp[-\tilde{\omega}^2\sigma_t^2] exp\left[-\frac{(x-\delta_0)^2 + 2\delta_1(x-\delta_0) + {\delta_1}^2\tilde{\omega}^2}{4\sigma_{x\omega_0}^2}\right]. \tag{5}$$

It can be observed from Eq. (5) that the term α_0 does not contribute to the irradiance field. The linear terms in $\tilde{\omega}$ give rise to a group delay (GD), where the coefficient α_1 produces a uniform temporal shift in pulse arrival time. Also, there is a **spatial** broadening induced by angular dispersion. The resultant instantaneous irradiance distribution $I_{out}(x,t)$, obtained as the modulus square of the inverse Fourier transform, can be expressed as follows:

$$I_{out}(x,t) \approx \exp\left[-\frac{(t-\alpha_1)^2}{2\sigma_t'^2}\right]\exp\left[-\frac{(x-\delta_0)^2}{4\sigma_x'^2}\right], \tag{6}$$

With $\sigma_t'^2 = \sigma_t^2(1 + (4\,\sigma_x^2\,\pi^2m^2)/(\sigma_t^2p^2{\omega_0}^2))$ and $\sigma_x'^2 = \sigma_{x\omega_0}^2(1 + (4\,\sigma_x^2\,\pi^2m^2)/(\sigma_t^2p^2{\omega_0}^2))$. Since the irradiance remains as a product of two expanded Gaussians functions, there is a temporal shift determined by α_1, and a spatial shift governed by δ_0. This spatial shift increases with the diffraction order m, and depends on the DMD micromirror spacing, p. As a result, a spatiotemporal deformation arises, characterized by a spatial broadening factor of $\sigma_x'^2/\sigma_{x\omega_0}^2$ and a temporal broadening factor of $\sigma_t'^2/\sigma_t^2$. This result is consistent with previous reports in the literature [42]. It should be emphasized that, in this theoretical treatment, non-linear phenomena inside the DMD—such as self-phase modulation occurring in the protective window—have not been considered, since under standard operating conditions these effects are negligible.

To experimentally observe this spatial broadening, we recorded the spatially dispersed beam using an infrared camera placed in the far-field of the DMD. In this configuration, the DMD acts as a diffraction grating, and the propagation to the far-field (Fraunhofer regime) performs the spatial mapping of the spectral components. The laser beam struck the DMD at normal incidence, with all micromirrors set to the ON state as shown in Fig. 5 (a). To clearly highlight the angular dispersion for different wavelengths, three spectral bandpass filters with central transmissions of 780 nm, 800 nm, and 820 nm were placed between the DMD and the screen (Fig. 5a). Initially, an image of the full spectrum of the light beam after being reflected by the DMD was obtained for comparison, as shown in Fig. 5 b (i). Then, the corresponding spectral traces on the screen were recorded, as shown in Fig. 5 b(ii)-5b(iv). The spectral bands exhibit similar spatial distributions but are clearly displaced relative to each other.

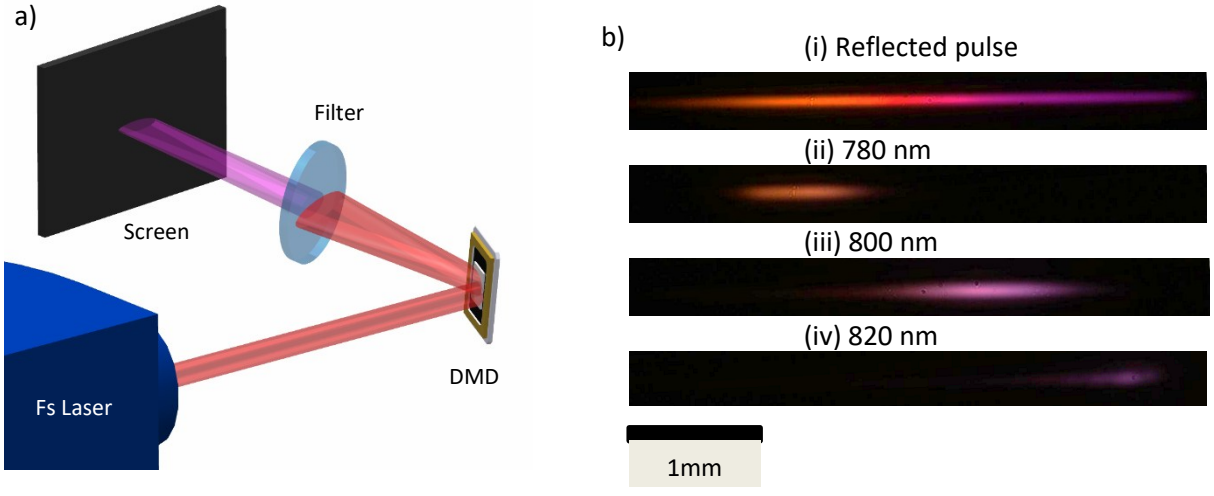

Fig. 5. (a) Schematic representation of the experimental setup. (b) Images illustrating the dispersion of the light spectrum captured by the infrared camera: (i) full pulse after reflection by the DMD, pulse after passing through (ii)780 nm, (iii) 800 nm, and (iv) 820 nm bandpass filters.

These findings reveal that the various wavelength components of the light are diffracted at different angles because of the wavelength-dependent diffraction properties of the micromirrors. This spatial separation of the spectral components results in lateral chromatic aberration. For ultrashort pulses, spatial wavelength dispersion directly affects the pulse's temporal characteristics. Because the spectral components are no longer confined to a single spatial point, their temporal overlap is greatly reduced, effectively elongating the pulse duration. This spectral-to-temporal mapping implies that, for Fourier transform-limited pulses, the pulse duration increases as a result of the chromatic dispersion introduced by diffraction. The temporal broadening becomes more pronounced as the diffracted pulse propagates over longer distances because the angular separation between wavelength components increases. As a consequence, the pulse loses its original temporal coherence, leading to a longer pulse duration. These results emphasise the need to incorporate an optical compensation system in DMD-based setups to effectively mitigate these diffraction-induced effects. Without such compensation, the temporal width may increase significantly, potentially compromising system performance in ultrashort pulse experiments. Additionally, the total optical diffraction efficiency of the DMD system depends on the fill factor of the micromirror array, the surface reflectivity of the micromirror, the transmission of the window and the diffraction efficiency. For the DLP7000 DMD used in our experiment, the central wavelength of the laser beam, and the aperture of the collection system, these values are nominally 92%, 88%, 95% (single pass), and 86%, respectively [36]. Taking all this factors into account, the total optical efficiency of the DMD system is 63%.

In conclusion, the DMD introduces modifications in the spatiotemporal structure of a pulsed laser. The GDD introduced by the DMD represents a minor effect for conventional pulse durations. However, since the DMD acts as a diffraction grating, the spatiotemporal propagation of the pulse is strongly affected by its diffractive nature. Thus, for short pulse durations, the implementation of adequate dispersion compensation must be carefully considered [43, 44].

4. Beam characterization through single-pixel imaging

SLM such as the DMD are key components in single-pixel imaging techniques (SPI). Based on the study presented in Section 2, it is possible to obtain images of ultrashort light pulses using a DMD without significantly reducing the beam energy or not reducing any. This imaging modality operates by sampling the object with a sequence of structured masks, while the total light intensity transmitted or reflected by each mask is recorded by a single-pixel (bucket) detector [45]. The final image is then numerically reconstructed from the photocurrent signal using computational algorithms. The simplicity of the sensing device enables efficient operation under low-light conditions unlike unconventional imaging techniques, which are rely primarily on pixelated sensors. Furthermore, this approach simplifies the measurement of the spatial distribution of multiple optical properties of the sample, such as its spectral content, in a direct approach. Moreover, single-pixel detectors can operate over a much broader spectral range than conventional cameras. The imaging process can be described by the following matrix–vector expression [46]:

$$\boldsymbol{y} = \mathrm{A}\boldsymbol{x} + \boldsymbol{\epsilon}, \quad (7)$$

where $\boldsymbol{x}$ represents the image to be reconstructed in a one-dimensional vector form, A is the measurement matrix that encodes the sequence of sampling masks in its rows, constructed with an orthonormal set of functions, and $\boldsymbol{y}$ is a vector containing the corresponding measurement sequence. The vector ϵ represents the noise present in the measurement process.

Given an object of dimension N (where N is the number of pixels), an appropriate mathematical basis, such as the Walsh-Hadamard basis, with this N dimensional space must be selected as the measurement basis. The inverse of the measurement matrix can then be computed for the recovery of the object, assuming low values of noise ($\boldsymbol{\epsilon} \sim 0$):

$$\boldsymbol{x} = \mathrm{A}^{-1}\boldsymbol{y}. \quad (8)$$

Certain bases are associated with fast and efficient digital transformation algorithms, making image reconstruction practical even for large image sizes. In particular, the Hadamard basis is well suited to DMD-based single-pixel imaging techniques because its binary nature allows full utilisation of the DMS's refresh rate. The Hadamard basis functions are orthogonal and take binary values of +1 or −1.The negative values can be encoded by considering that the measurement process in Eq. (8) is linear and that the Hadamard matrix can be expressed as H = H+ − H−, where H+ is the Hadamard matrix with all entries of the value −1 changed to 0, and H− is its complementary matrix. With these properties, the measurement can be expressed as a two-step process: the H+ pattern corresponding to each element of the $\mathbf{A_i}$ basis is measured, followed by its complementary H− pattern; then, the two measured values are subtracted to measure each individual coefficient of $\boldsymbol{y_i}$. This differential measurement process suppresses parasitic signals, such as ambient light or slow fluctuations of the light source.

For the experimental implementation, the pulsed laser beam from the Ti:Sapphire laser (PRO-Compact) was incident on a DMD, where the sequence of Walsh-Hadamard patterns defined by matrix **A** was encoded. The scanning patterns were encoded as binary images with a resolution of 128 x 128 pixels, using 256 x 256 DMD micromirrors, covering an area of $3.5 \times 3.5\ \mathrm{mm}^2$. To properly scan the laser beam profile, the laser beam was aligned to propagate normal to the DMD surface, as shown in Fig. 6(a). For each scanning pattern, the reflected light, emerging at an angle of 24º from the DMD, was collected by a pair of lenses in a close-to-afocal configuration with focal lengths of 125 mm and 50 mm. As there is an image relationship between the DMD plane and the photodiode plane, and a demagnified image of the light spot at the DMD is projected onto the active area of the photodiode, it is not necessary to take into account the spatial chirp introduced by the DMD. The light beam was focused onto a photodiode (DET36A2 Thorlabs). The photocurrent signal was digitised by a data acquisition board, which generated the measurement vector $\boldsymbol{y}$. The irradiance map of the light beam was reconstructed by applying a fast inverse Hadamard transform, according to Eq. (8). To reduce the noise arising from the laser fluctuations, several measurements were averaged. The final image was obtained using 32768 patterns, with the DMD operated at a frequency limited by the laser repetition rate of 1 kHz, which obtained one pattern measurement for each pulse. The reconstructed irradiance distribution, expressed in arbitrary units, has a FWHM of 0.84 mm as shown in Fig. 6 (b).

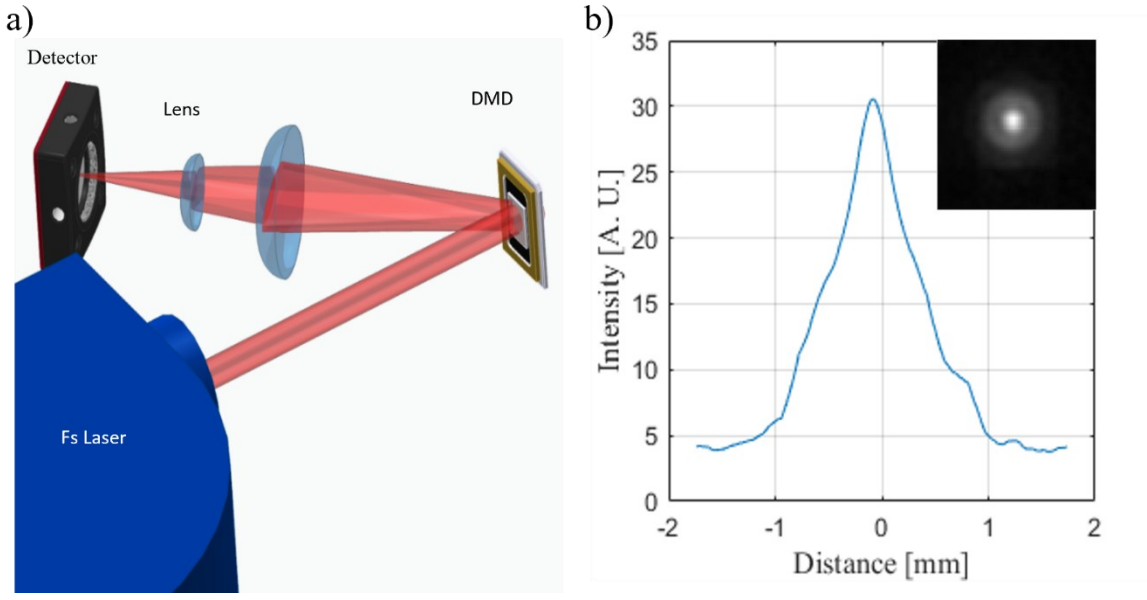

Fig. 6. (a) Schematic diagram of the optical setup showing the optical path of the light beam reflected by the DMD and focused by a pair of lenses onto the photodiode. (b) Horizontal intensity profile of the light beam along the axis corresponding to the point of maximum intensity. The inset shows the two-dimensional (2D) irradiance distribution reconstructed using the single-pixel imaging technique.

5. Conclusion

This study provides substantial technical understanding of the DMD laser interaction to further improve its utilisation in diverse optical applications. In this work, the damage fluence of a DMD under ultrashort pulsed laser irradiation was first calculated, to ensure its safety operation in ultrafast laser systems. Experimental results showed that the damage threshold fluence of the DMD is $0.12 \pm 0.02\,\mathrm{J/cm^{-2}}$. Moreover, the GDD introduced by the DMD was evaluated from the nominal characteristics of its components, and was measured to be 190 fs^2. This value was further verified through autocorrelation measurements.

The analysis also included the diffractive properties and dispersion effects that result from the interaction of ultrashort pulses with the DMD. Theoretical modelling detailed how the DMD affects the pulses through diffraction, showing a spatiotemporal shift and spatial broadening that depend on the diffraction order. Experimental verification was carried out by observing the dispersed pulse spectrum projected on a screen and by measuring the spectra before and after the interaction of the ultrashort pulses with the DMD, showing this significant spatial broadening of the different wavelengths.

Finally, the versatility of the DMD as an imaging device was demonstrated in which the spatial irradiance distribution of the pulse was reconstructed using single-pixel imaging techniques. Overall, the results demonstrate that the DMD is a promising platform for producing highly accurate and efficient images of ultrashort light pulses.

Acknowledgments

The authors are very grateful to the "Servei Central d'Instrumentació Científica" (SCIC), Universitat Jaume I, for the use of laser facilities.

Funding

We acknowledge Agencia Estatal de Investigación, Spain, for the project PID2022-142907OB-I00 funded by MICIU/AEI/10.13039/501100011033 and "ERDF/EU". Funding from the Generalitat Valenciana (CIPROM/2023/44, GRISOLIAP/2021/178) is also acknowledged.

Conflicts of interest:

The authors declare no conflict of interest in regards to this article.

Data availability statement:

Data underlying the results presented in this paper are not publicly available at this time but maybe obtained from the authors upon reasonable request.

Author contribution statement:

Conceptualization, G. Mínguez-Vega. Methodology, Mitzi Ordoñez-Perez and Pedro J. Clemente-Pesudo. Formal Analysis, Mitzi Ordoñez-Perez and G. Mínguez-Vega. Writing – Original Draft Preparation, Mitzi Ordoñez-Perez and Enrique Tajahuerce. Writing – Review & Editing, Francis Rey U. Cortes and G. Mínguez-Vega. Supervision, G. Mínguez-Vega and Enrique Tajahuerce. Project Administration, G. Mínguez-Vega. Funding Acquisition and Visualization, Jesús Lancis.

References

1. Zhang Z, Gao Y, Wang X, et alSelective Generation of Laser Transverse Modes by Gain Regulation With a Digital Micromirror Device. IEEE Photonics Technology Letters 34, 420–423. (2022) https://doi.org/10.1109/LPT.2022.3164417

2. Sheikh M, Riza NA Demonstration of pinhole laser beam profiling using a digital micromirror device. IEEE Photonics Technology Letters 21, 666–668 (2009). https://doi.org/10.1109/LPT.2009.2016113

3. Soldevila F, Durán V, Clemente P, et al Phase imaging by spatial wavefront sampling. Optica 5, 164. (2018) https://doi.org/10.1364/optica.5.000164

4. Loriot V, Mendoza-Yero O, Pérez-Vizcaíno J, et al Fresnel phase retrieval method using an annular lens array on an SLM. Appl Phys B 117, 67–73. (2014) https://doi.org/10.1007/s00340-014-5799-9

5. Weiner AM Femtosecond pulse shaping using spatial light modulators. Review of Scientific Instruments 71,1929–1960. (2000) https://doi.org/10.1063/1.1150614

6. Mendoza-Yero O, Loriot V, Pérez-Vizcaíno J, et al Programmable quasi-direct space-to-time pulse shaper with active wavefront correction. Opt Lett 37, (2012). https://doi.org/https://doi.org/10.1364/OL.37.005067

7. Köhler J, Wollenhaupt M, Bayer T, et al Zeptosecond precision pulse shaping. J Chem Phys 111, 10934–10956. (2011) https://doi.org/https://doi.org/10.1364/OE.19.011638

8. Salter PS, Booth MJ Adaptive optics in laser processing. Light Sci Appl 8, 1–16. (2019) https://doi.org/10.1038/s41377-019-0215-1

9. Torres-Peiró S, González-Ausejo J, Mendoza-Yero O, et al Parallel laser micromachining based on diffractive optical elements with dispersion compensated femtosecond pulses. Opt Express 21, 31830. (2013) https://doi.org/10.1364/oe.21.031830

10. Tross J, Kolliopoulos G, Trallero-Herrero CA Self referencing attosecond interferometer with zeptosecond precision. Opt Express 27, 22960. (2019) https://doi.org/10.1364/oe.27.022960

11. Mendoza-Yero O, Carbonell-Leal M, Doñate-Buendía C, et al Diffractive control of 3D multifilamentation in fused silica with micrometric resolution. Opt Express 24, 15307. (2016) https://doi.org/10.1364/oe.24.015307

12. Villoresi P, Bonora S, Pascolini M, et al Optimization of high-order harmonic generation by adaptive control of a sub-10-fs pulse wave front. Opt Lett 29, (2004) https://doi.org/https://doi.org/10.1364/OL.29.000207

13. Krenn M, Handsteiner J, Fink M, et al Twisted light transmission over 143 km. Proc Natl Acad Sci U S A 113, 13648–13653. (2016) https://doi.org/10.1073/pnas.1612023113

14. Zhuang Z, Ho HP Application of digital micromirror devices (DMD) in biomedical instruments. J Innov Opt Health Sci 13 (2020). https://doi.org/10.1142/S1793545820300116

15. Harrison J, Naidoo D, Forbes A, Dudley A Progress in high-power and high-intensity structured light. Adv Phys X 9, (2024) https://doi.org/10.1080/23746149.2024.2327453

16. Y. Yang, A. Forbes, and L. Cao, A Review of Liquid Crystal Spatial Light Modulators: Devices and Applications, Opto-Electronic Science.2,8, (2023) https://doi.org/10.29026/oes.2023.230026.

17. Toporovsky V, Samarkin V, Sheldakova J, et al Water-cooled stacked-actuator flexible mirror for high-power laser beam correction. Opt Laser Technol 144, (2021) https://doi.org/10.1016/j.optlastec.2021.107427

18. Soloviev A, Kotov A, Martyanov M, et al Improving focusability of post-compressed PW laser pulses using a deformable mirror. Opt Express 30, 40584. (2022) https://doi.org/10.1364/oe.471300

19. Furieri T, Bassi A, Bonora S Large field of view aberrations correction with deformable lenses and multi conjugate adaptive optics. J Biophotonics 16, (2023) https://doi.org/10.1002/jbio.202300104

20. Turtaev S, Leite IT, Mitchell KJ, et al Comparison of nematic liquid-crystal and DMD based spatial light modulation in complex photonics. Opt Express 25, 29874. (2017) https://doi.org/10.1364/oe.25.029874

21. Geng Q, Wang D, Chen P, Chen SC Ultrafast multi-focus 3-D nano-fabrication based on two-photon polymerization. Nat Commun 10 (2019) https://doi.org/10.1038/s41467-019-10249-2

22. Wang P, Liang J, Wang L V. Single-shot ultrafast imaging attaining 70 trillion frames per second. Nat Commun 11 (2020) https://doi.org/10.1038/s41467-020-15745-4

23. Cheng J, Gu C, Zhang D, Chen S-C High-speed femtosecond laser beam shaping based on binary holography using a digital micromirror device. Opt Lett 40, 4875. (2015) https://doi.org/10.1364/ol.40.004875

24. Gu C, Chang Y, Zhang D, et al Femtosecond laser pulse shaping at megahertz rate via a digital micromirror device. Opt Lett 40, 4018. (2015) https://doi.org/10.1364/ol.40.004018

25. Gu C, Zhang D, Chang Y, Chen S-C Digital Micromirror device-based ultrafast pulse shaping for femtosecond laser. Opt Lett 40, 2870. (2015) https://doi.org/10.1364/ol.40.002870

26. Gunnar Ritt Michael Koerber, Bernd Eberle, Laser-induced damage threshold of camera sensors and microoptoelectromechanical systems. Optical Engineering 56 (2017) https://doi.org/10.1117/1.OE.56.3.034108.

27. Wellershoff S-S, Hohlfeld J, Güdde J, Matthias E The role of electron–phonon coupling in femtosecond laser damage of metals. Appl Phys A Mater Sci Process 69, S99–S107. (1999) https://doi.org/10.1007/s003399900305

28. Schwarz B, Ritt G, Eberle B, Impact of threshold assessment methods in laser-induced damage measurements using the examples of CCD, CMOS, and DMD. Appl Opt 60, F39. (2021) https://doi.org/10.1364/ao.423791

29. Perrie W, Gill M, Robinson G, et al, Femtosecond laser micro-structuring of aluminium under helium. Appl Surf Sci 230, 50–59. (2004) https://doi.org/10.1016/j.apsusc.2003.12.035

30. Bashir S, Rafique MS, Husinsky W, Identification of non-thermal and thermal processes in femtosecond laser-ablated aluminum. Radiation Effects and Defects in Solids 168, 902–911. (2013) https://doi.org/10.1080/10420150.2013.784911

31. P. F. Van Kessel, L. J. Hornbeck, R. E. Meier, and M. R. Douglass, A MEMS-Based Projection Display, Proceedings of the IEEE, 86,8 (1998). https://doi.org/10.1109/5.704274

32. Texas Instruments. Digital Micromirror Device Thermal Considerations Including Pulsed Optical Sources: application note [Internet]. Dallas (TX): Texas Instruments; 2024 Jan. Technical report No. DLPA027B. Revised 2024 Apr [cited 2025 Nov 28]. Available from: https://www.ti.com/lit/an/dlpa027b/dlpa027b.pdf?ts=1764273477795

33. Stefan Nolte, in Ultrafast Lasers: Technology and Applications, edited by Fermann ME, Galvanauskas A, and Sucha G (Marcel Dekker, New York, 2003), pp. 376–379

34. Zhang J, Chen Y, Hu M, Chen X An improved three-dimensional two-temperature model for multi-pulse femtosecond laser ablation of aluminum. J Appl Phys 117, (2015) https://doi.org/10.1063/1.4907990

35. Jm L Simple technique for measurements of pulsed gaussian-beam spot sizes. Opt Lett 7:196. (1982) https://doi.org/10.1364/ol.7.000196

36. Texas Instruments. DLP7000 DLP® 0.7 XGA 2× LVDS Type A DMD: technical datasheet [Internet]. Dallas (TX): Texas Instruments; (2012) Aug. Technical report No. DLPS029B. Updated 2023 Apr. Cited 2025 Nov 28. Available from: https://www.ti.com/lit/ds/symlink/dlp7000.pdf

37. Dudley D, Duncan WM, Slaughter JW Emerging Digital Micromirror Device (DMD) applications. Proceedings of SPIE. (2003) https://doi.org/10.1117/12.480761

38. Edmund Optics. Metallic Mirror Coatings: application note [Internet]. Barrington (NJ): Edmund Optics; n.d. [cited 2025 Nov 28]. Available from: https://www.edmundoptics.com/knowledge-center/application-notes/optics/metallic-mirror-coatings/

39. Newport Corporation. The Effect of Dispersion on Ultrashort Pulses: application note [Internet]. Newport (CA): Newport Corporation; n.d. [cited 2025 Nov 28]. Available from: https://www.newport.com/n/the-effect-of-dispersion-on-ultrashort-pulses

40. Sune Svanberg, Wolfgang Demtroder in Springer Handbook of Lasers and Optics, edited by Träger F, 2nd edn. (Springer, Berlin, 2012), pp. 1047–1056.

41. Siegman AE, in Lasers, edited by University Science Books, 1st edn. (University Science Books, Mill Valley, 1986), p. 807

42. G. Mínguez-Vega, E. Tajahuerce, M. Fernández-Alonso, V. Climent, J. Lancis, J. Caraquitena, and P. Andrés, Dispersion-compensated beam-splitting of femtosecond light pulses: Wave optics analysis, Opt Express 15 pp. 278-288 (2007). https://doi.org/10.1364/OE.15.000278.

43. Martínez-Cuenca R, Martínez-León L, Lancis J, et al High-visibility interference fringes with femtosecond laser radiation. Opt Express 17, 23016. (2009) https://doi.org/10.1364/OE.17.023016

44. L. Martínez-León, P. Clemente, E. Tajahuerce, G. Mínguez-Vega, O. Mendoza-Yero, M. Fernández-Alonso, J. Lancis, V. Climent, and P. Andrés, Spatial-chirp compensation in dynamical holograms reconstructed with ultrafast lasers, Appl Phys Lett 94, (2009). https://doi.org/10.1063/1.3063047.

45. M. P. Edgar, G. M. Gibson, and M. J. Padgett, Principles and Prospects for Single-Pixel Imaging, Nature Photonics. 13, 13-20 (2019) https://doi.org/10.1038/s41566-018-0300-7.

46. Armin M. J. Lenz, Single-Pixel Computational Imaging: Application to Fluorescence and Diffuse Optical Imaging, thesis, Universitat Jaume I, (2024). https://doi.org/10.6035/14104.2024.716126.